ACS APPLIED MATERIALS & INTERFACES
Research Article
www.acsami.org

Engineering Efficient Thermoelectrics from Large-Scale Assemblies of Doped ZnO Nanowires: Nanoscale Effects and Resonant-Level Scattering

Lance Brockway,[†] Venkata Vasiraju,[‡] Mahendra K. Sunkara,[§] and Sreeram Vaddiraju*,[†,‡]

[†]Artie McFerrin Department of Chemical Engineering, Texas A&M University, 3122 TAMU, College Station, Texas 77843, United States

[‡]Materials Sciences and Engineering Department, Texas A&M University, 3003 TAMU, College Station, Texas 77843, United States

[§]Department of Chemical Engineering, University of Louisville, 106 Ernst Hall, Louisville, Kentucky 40292, United States

Ⓢ *Supporting Information*

ABSTRACT: Recent studies focusing on enhancing the thermoelectric performance of metal oxides were primarily motivated by their low cost, large availability of the component elements in the earth's crust, and their high stability. So far, these studies indicate that *n*-type materials, such as ZnO, have much lower thermoelectric performance than their *p*-type counterparts. Overcoming this limitation requires precisely tuning the thermal and electrical transport through *n*-type metal oxides. One way to accomplish this is through the use of optimally doped bulk assemblies of ZnO nanowires. In this study, the thermoelectric properties of *n*-type aluminum and gallium dually doped bulk assembles of ZnO nanowires were determined. The results indicated that a high zT of 0.6 at 1000 °C, the highest experimentally observed for any *n*-type oxide, is possible. The high performance is attributed to the tailoring of the ZnO phase composition, nanostructuring of the material, and Zn-III band hybridization-based resonant scattering.

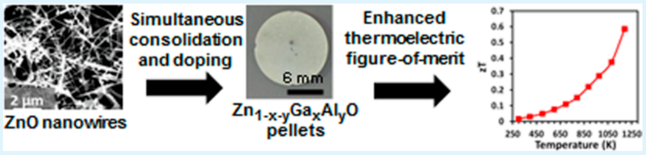

KEYWORDS: *zinc oxide, thermoelectrics, resonance, nanowires, hybridization*

INTRODUCTION

Thermoelectric generators (TEGs) are solid state devices that convert heat into electricity. The efficiency of thermoelectric materials composing the generators is gauged by their dimensionless figure of merit, zT, given by zT = $(S^2\sigma)/(\kappa_e + \kappa_L)T$, where S is the Seebeck coefficient, σ is the electrical conductivity, T is the absolute temperature, and κ_e and κ_L are the electronic and lattice contributions to the thermal conductivity, respectively.[1] Although the efficiency of thermoelectric materials and devices has improved considerably in the past two decades, they still lag behind conventional heat engines.[2] Additionally, state-of-the-art thermoelectric generators are currently made of rare and toxic materials. These limitations make thermoelectric devices prohibitive for most terrestrial applications and are currently limited for use in specialty applications, such as space exploration and remote power systems.[2,3]

An ideal thermoelectric material has electrical transport properties of a heavily doped semiconducting crystal and the thermal conductivity of a glass.[4] However, in band-type semiconductors, the Seebeck coefficient and electrical conductivity are coupled disproportionally with carrier concentration, and the Wiedemann−Franz law proportionally couples σ and κ_e.[5] These restrictions make engineering high-efficiency thermoelectric materials very difficult and have restricted the zT values of commercial materials to ∼1.[2] A possible pathway for increasing the zT of materials requires reducing the lattice thermal conductivity via phonon scattering at boundaries and interfaces. This can be achieved by increasing the number of interfaces via nanostructuring.[6] Relative to other nanomorphologies, single-crystalline nanowires offer enhanced electrical conduction due to fewer interfaces and single-crystalline electron conduction pathways.[7,8] Therefore, the potential for obtaining the highest possible zT for a given optimally doped material exists when it is synthesized in single-crystalline nanowire form.

Many reports in the literature, both theoretical[9] and experimental,[10] have indicated enhanced thermoelectric performance of materials in the single-crystalline nanowire form. More specifically, 50-fold[11] and 100-fold[12] increases in the zT of silicon nanowires have been reported. Despite all these recent achievements, there are very few attempts to fabricate nanowire-bulk modules to determine if individual nanowire properties extend to bulk devices, which could potentially be useful on an industrial scale.[13]

Over the past two decades, metal oxides have become viable thermoelectric materials due to their low cost, elemental abundance in the earth's crust,[14] low toxicity,[15] and high stability in oxidizing environments relative to other thermoelectric materials.[15] Many *p*-type oxide semiconductor materi-

Received: April 17, 2014
Accepted: August 11, 2014
Published: August 11, 2014

dx.doi.org/10.1021/am5023489 | *ACS Appl. Mater. Interfaces* 2014, 6, 14923−14930

als, such as $Ca_3Co_4O_9$ with a high zT of 0.61[16] and Na_xCoO_2 with a high zT of 0.92,[17] have been shown to have efficiencies on par with current commercial materials. Contrarily, many n-type oxides have yet to exhibit such performance. So far, the state-of-the-art known *n*-type oxide thermoelectric materials are $SrTiO_3$, with a maximum zT of 0.37,[18] and ZnO alloys doped[19,20] and codoped,[21,22] with a highest measured zT of 0.52.[23] The aim of this paper is to combine the superior thermoelectric properties of the dually alloyed ZnO material composition with nanowire morphology to increase the zT of the alloy. It will be demonstrated that the resonant scattering of carriers in conjunction with nanostructuring will further increase the zT of the ZnO alloys to the highest ever experimentally reported for an *n*-type oxide.

■ RESULTS AND DISCUSSION

a. Materials Characterization. X-ray diffraction (XRD) analysis (Figure 1) indicated the formation of both aluminum and gallium spinels in all dually doped ZnO samples. The compositions shown in Figure 1, $Zn_{96}Al_3GaO_{100}$, $Zn_{96}Al_2Ga_2O_{100}$, $Zn_{97}Al_2GaO_{100}$, and $Zn_{98}AlGaO_{100}$, correspond to the respective atomic compositions of the raw materials used to fabricate each sample. These compositions will be used to identify the samples throughout the paper. The XRD analysis indicated no presence of unreacted gallium and aluminum oxide phases in the samples, and that alumina and the gallium oxide reacted with ZnO. Subsequently, some of the aluminum and gallium supplied precipitated as spinel from the alloy with compositions of $(ZnO)_x(Al_2O_3)_y$ and $(ZnO)_x(Ga_2O_3)_y$, respectively, at all the concentrations studied. These solubility limits are less than the independent solubility limit of both aluminum and gallium in zinc oxide,[24] and contradict a previous claim that dual doping can increase the solubility limit of group III metals in zinc oxide.[23] It is more likely in the previous report that peak broadening due to lattice distortions by Ga doping[25] was responsible for engulfing the precipitant peaks. It has also been shown that as the temperature increases, spinel formation will be much faster due to faster diffusion kinetics.[26] Despite the relatively low temperature of 1200 °C used during pressing, the local temperature at the nanowire grain boundaries will be very high when using spark plasma sintering (SPS) due to their high resistivity and consequential Joule heating.[27] Therefore, more spinel compound will form than would be expected at 1200 °C in 5 min. Representative, scanning electron micrographs of the ZnO nanowires before pressing (Figure 2a) and the pellet after pressing (Figure 2b) indicate that the pellets are phase-pure up to the maximum allowed resolution of the backscattered electron detector. Furthermore, high-resolution transmission electron microscopy (HRTEM) images of the nanowires before pressing (Figure 2c) indicate that they are single crystalline and grow in the [001] direction. Destructive analysis on the pellets was performed to determine if the single-crystalline nanowire morphology still exists in the pellet. Although the nanowires were broken into pieces, the HRTEM analysis indicated that the anisotropic crystalline pieces of ZnO with [001] growth directions were still recoverable (Figure 2d). The grain morphology was maintained during sintering due to SPS minimizing the grain growth relative to other sintering methods.[27] The use of nanowires and nanoparticles as building-blocks in conjunction with SPS increased the reaction rate and permitted even shorter sintering times relative to the bulk. This is due to the higher specific surface area and shorter required diffusion distances in nanomaterials.[28] Therefore, the 5 min sintering time was sufficient to completely react and consolidate the nanowires without destroying their morphology.

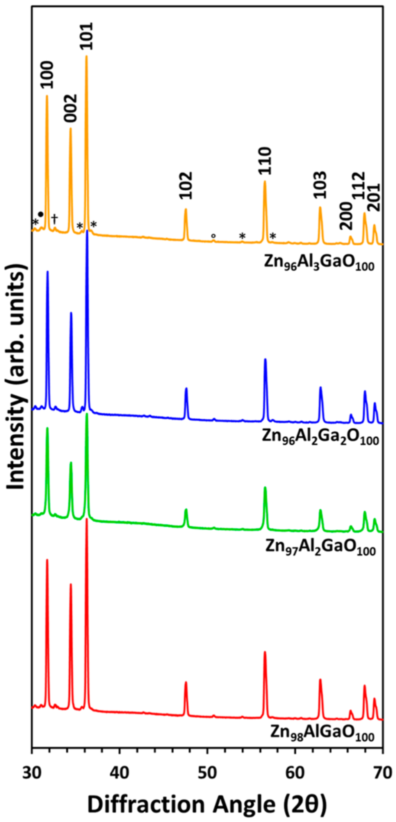

Figure 1. XRD spectrographs of the dually doped ZnO nanowire pellets of various nominal compositions employed in this study. After consolidation, the primary phase found in all the pellets was ZnO. Furthermore, the samples containing gallium indicated the formation of $ZnGa_2O_4$ (∗) spinel and $(ZnO)_{13}(Ga_2O_3)_2$ (•) in increasing quantities as more gallium was added. Additionally smaller amounts $ZnAl_2O_4$ (∘) spinel and $(ZnO)_3(Al_2O_3)$ (†) are present.

b. Electronic Transport. Both aluminum and gallium have previously been utilized as electron donors in ZnO.[20,23,29] The *n*-type conductivity was achieved by substituting Al or Ga with 3 valence electrons for Zn with 2 valence electrons in the wurtzite lattice. For every Zn atom replaced with a group III element, 1 additional electron is donated into the conduction band, as can be seen in the charge balance (eq 1).

$$Zn^{2+} = III^{3+} + e^- \tag{1}$$

The known self-compensation of *n*-type carriers by zinc vacancies does not occur before the solubility limits of Al or Ga, resulting in the maximum solubility of the dopants to solely determine the carrier concentration of the samples.[29] The temperature dependence of electron mobility (μ_H) calculated from the resistivity (ρ) and Hall coefficient (R_H) can be seen in Figure 3a. For materials where mobility is limited by phonon scattering, $\mu_H \propto T^{-x}$, where x is 1 for degenerate semiconductors and 1.5 for nondegenerate semiconductors. A power law fit to the curves yields a trend with x slightly larger than 1, consistent with a degenerate semiconductor. This slight deviation from theory can be attributed to other scattering mechanisms playing a minor role in the electron transport.

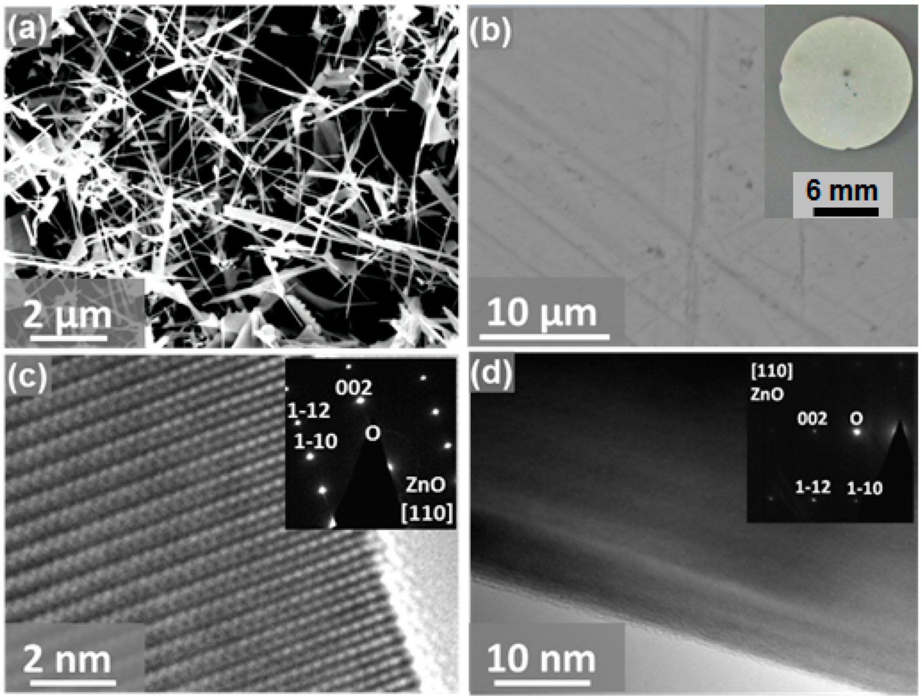

Figure 2. (a) Scanning electron micrograph of the as-synthesized ZnO nanowires employed in this study. (b) Backscatter SEM image of the nanowire pellet after densification in the SPS indicating phase purity on the macroscale. The inset is an optical micrograph of one of the pellets fabricated. (c) HRTEM of an individual ZnO nanowire showing that it is single crystalline and grew along the [001] direction. (d) HRTEM of a broken ZnO nanowire obtained by crushing the consolidated nanowire pellet. This analysis indicated that single-crystalline nanowire-shaped grains with the same growth direction are retained within the pellet after compaction.

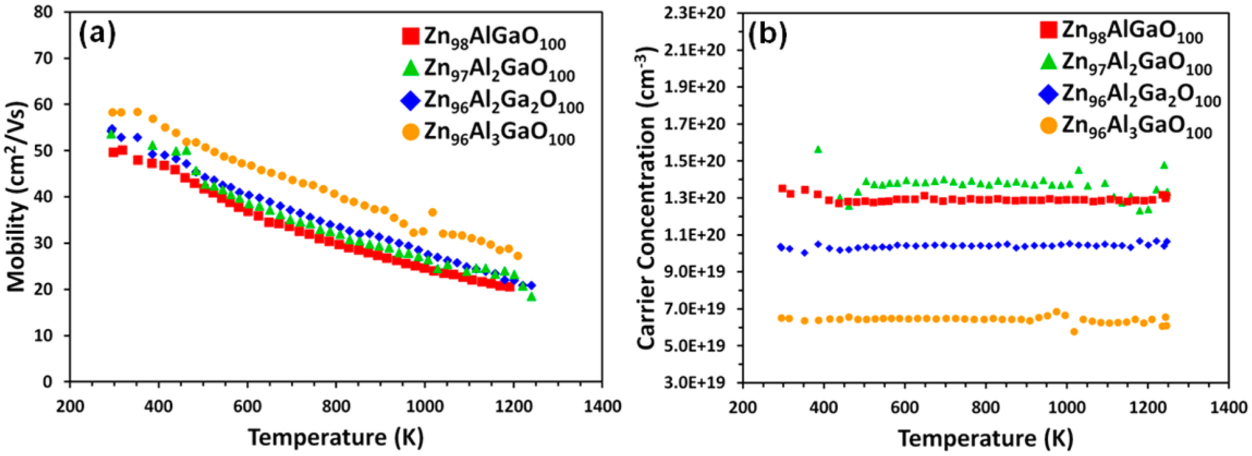

Figure 3. Plots indicating the variation of the (a) carrier mobility and (b) carrier concentration for various dually doped zinc oxide nanowire pellets with temperature. The decay in the mobility is proportional to T^{-1}, consistent with that expected of degenerate semiconductors in which acoustic phonon scattering limits the carrier mobility. The carrier concentration is independent of temperature for each sample, characteristic of degeneracy in the samples.

Carrier concentration (n_H) was also calculated from the Hall coefficient and plotted versus temperature (Figure 3b). The resulting plots indicate that carrier concentration is independent of temperature and constant throughout the entire measurement, further confirming the degenerate semiconductor behavior. The group III element solubility for each sample is presented in Table S1 (Supporting Information). The calculated carrier concentrations at the pressing conditions are consistent with the phase diagram in this region, which indicates that the equilibrium solubility of Al in ZnO is 0.2% at 1250 °C and 0.5% at 1400 °C.[30] Therefore, most of the dopant added to the ZnO is inactive and must have precipitated out as gallium and aluminum spinel phases. This was confirmed by the XRD analysis depicted in Figure 1. All the carrier concentrations being less than the maximum values reported of 8×10^{20} and 3.7×10^{20} cm^{-3} for aluminum[31] and gallium[32] doped ZnO, respectively, confirms the fact.

Electrical resistivity measurements were performed simultaneously with the Hall coefficient measurements, and the resistivity was observed to increase linearly with temperature (Figure 4a). It is important here to mention that pellets of pristine ZnO nanowires were also fabricated. However, they were found to be highly resistive, well above the measurement range of our instrumentation. Therefore, no data from pristine

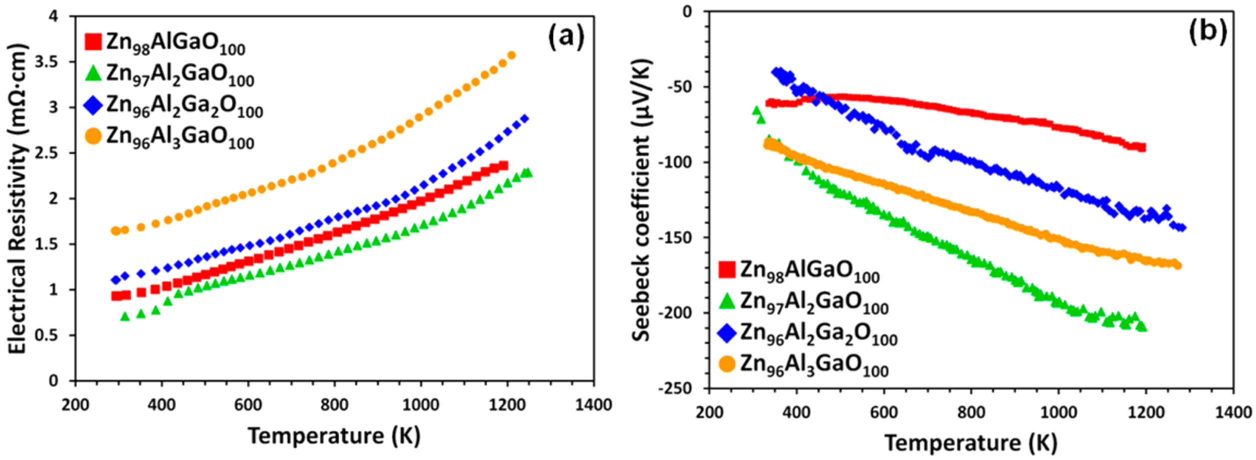

Figure 4. Plots indicating the variation of (a) electrical resistivity and (b) Seebeck coefficient of the dually doped ZnO samples with temperature. All samples, except $Zn_{97}Al_2GaO_{100}$, exhibited an inverse proportionality between the Seebeck coefficient and electrical resistivity, characteristic of classical degenerate semiconductors. The lone discrepancy is attributed to resonant-level scattering of electrons in $Zn_{97}Al_2GaO_{100}$.

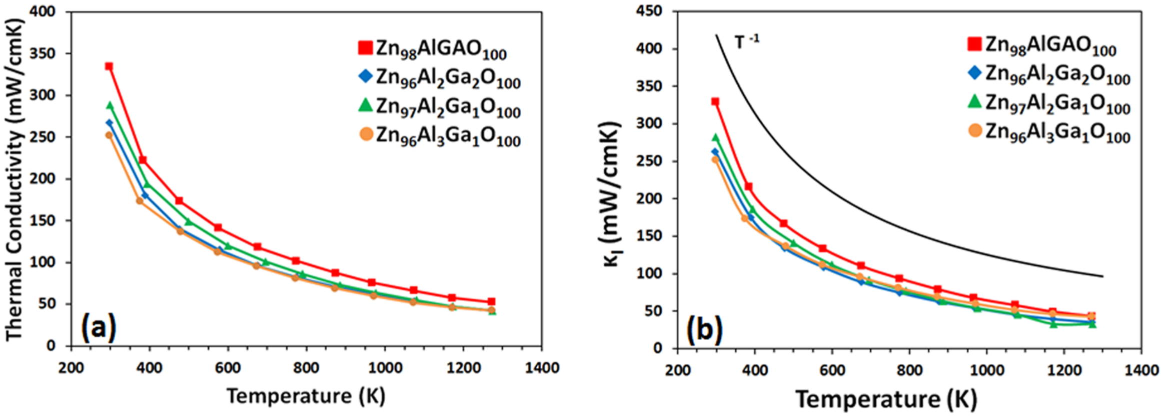

Figure 5. (a) Plot indicating the variation of the thermal conductivity of the dually doped ZnO nanowire pellets with temperature. The data indicated a reduction in the thermal conductivity with an increase in the dopant concentration. This is attributed to the creation of more phonon scattering centers from nanoparticle precipitants. (b) Plot indicating the variation of the lattice thermal conductivity, κ_L, with temperature. The lattice thermal conductivities of all the samples decayed with temperature proportional to T^{-1}, as expected of degenerate semiconductors where U-processes dominate phonon scattering.

ZnO nanowire pellets were included. The Seebeck coefficient was also measured up to 1000 °C and, with all samples, has an approximately linear temperature dependence (Figure 4b). All samples have a Seebeck coefficient that is inversely proportional to their carrier concentration and follows normal band-behavior dominated by acoustic phonon scattering, with the exception of $Zn_{97}Al_2GaO_{100}$. This composition seems to violate the classical band-transport theory which predicts an inverse proportionality between carrier concentration and Seebeck coefficient for a given material. Such a behavior is expected due to resonant electron scattering.[33−35] It has previously been reported that as the concentration of aluminum increases, the impurity band moves from a donor state with an ionization energy of 120 meV[36] to well within the conduction band.[37] Additionally, the gallium impurity band has been predicted to be inside the conduction band.[38] These impurity energy levels in the conduction band alone could potentially resonantly scatter the host semiconductor's electrons, but would have weak effects above ~300 K due to acoustic phonon scattering dominating transport. The Seebeck coefficient of the 2% Al, 1% Ga sample is enhanced independent of temperature, and makes the temperature-dependent scattering of electrons by the impurity band improbable. Contrarily, another mechanism that could cause resonant scattering and is more dependent on the band-structure and less on temperature involves the hybridization of the host band-structure with that of the impurity band. In this case, the impurity bands have plane-wave-like wave functions that correspond with those of the host structure and allow the impurity electrons to enhance the power factor.[35] The degree of hybridization between the bands must be balanced to achieve maximum resonance. If the degree of overlap is too much, then the impurity band will behave like the host, and no power factor enhancement will be observed. On the other hand, too little overlap will result in high-Seebeck localized states that do not contribute to the overall performance of the material.[35] When this theory is applied to the dually doped ZnO system, the group III valence s-bands could hybridize with the ZnO conduction band, resulting in an increased effective electron mass. This resonant phenomenon has not previously been observed in individually Al or Ga doped ZnO systems, but unexplainable Seebeck enhancements have been seen previously in other dually doped samples[23] in addition to this study. Resonance donor states have also been observed in many other transition metal-doped II−VI compounds.[39] If the conduction band is hybridized, a changed effective mass would be observed; these values can be approximated using the single parabolic band (SPB) model.[40−42] Detailed information about the SPB calculations is included in the Supporting Information. Theoretical estimation of lowest and highest nominally doped samples, $Zn_{98}AlGaO_{100}$ and $Zn_{96}Al_3GaO_{100}$, indicated that they have an effective mass of 0.29 m_e and 0.26 m_e, respectively, similar to that of pure ZnO (0.29 m_e).[43] However, the two other samples studied, $Zn_{96}Al_2Ga_2O_{100}$ and $Zn_{97}Al_2GaO_{100}$, had effective masses of 0.41 m_e and 0.90 m_e. Table S2 (Supporting Information) summarizes the properties of the samples at 1073 K for direct comparison. The large increase in the effective mass results in a much larger Seebeck coefficient, and consequently, larger power factor of the optimally performing sample ($Zn_{97}Al_2GaO_{100}$). The variation of effective mass with carrier concentration indicates a breakdown in the SPB model, and that an alternate transport behavior is occurring. Hybridization of the impurity states with the conduction band is a probable scenario that explains the enhanced thermopower and anomalies with the SPB model.

c. Thermal Transport. The thermal conductivity of the pellets was calculated from the values of thermal diffusivity (α), density (ρ), and specific heat (C_p) using the following relationship: $\kappa = \alpha\rho C_p$. It was observed that as the amount of group III dopant increased in the sample, the thermal conductivity was lowered (Figure 5a). A maximum 4-fold decrease in thermal conductivity relative to that of single-crystalline ZnO is observed in these dually doped samples at 300 K.[44] In addition, it was observed that nanostructuring led to a decrease in the thermal conductivity. Use of nanostructures in the fabrication of the pellets led to at least a 25% reduction in the thermal conductivity relative to their bulk counterparts at 1073 K.[23] Overall, alloy scattering coupled with boundary scattering at the nanowire interfaces within the consolidated sample can be attributed to these large decreases in thermal conductivity. The precipitated spinel phases also provide more interfaces and increase the phonon scattering within the samples as can be seen in the XRD (Figure 1) and TEM (Figure S1, Supporting Information) analyses, thereby further reducing the thermal conductivity of the samples. From these results, it can be concluded that this strategy for making ZnO alloy nanostructured thermoelectrics results in the lowest thermal conductivity reported to date for ZnO-based systems. The electronic thermal conductivity, κ_e, was calculated using the Wiedemann−Franz law, $\kappa_e = LT/\rho$, where L is the Lorenz number, T is the absolute temperature, and ρ is the electrical resistivity. For degenerate semiconductors, the Lorenz number varies as a function of the Fermi level resulting in values of up to 10 orders of magnitude less than the free electron value of 2.44×10^{-8} WΩ K^{-2} expected for metals.[42] Therefore, it is necessary to calculate these values for each composition due to varying chemical potentials. Assuming Umklapp scattering as the dominant process for this material system, the single parabolic band model can be used to calculate the Lorenz numbers as shown previously.[40,42] This results in values of L ranging from 1.66×10^{-8} to 2.08×10^{-8} WΩ K^{-2}, much less than that for metals. The lattice thermal conductivity, κ_L, can be calculated from $\kappa = \kappa_e + \kappa_L$ and is plotted in Figure 5b as a function of temperature. Umklapp-processes are confirmed as the dominant phonon scattering mechanism as the lattice thermal conductivities are proportional to T^{-1} for all carrier concentrations. The slight deviations from this value can be attributed to alloy and interfacial scattering, specifically at lower temperatures where U-processes are not as dominant.

d. Thermoelectric Figure of Merit. Plots indicating the variation of zT with temperatures for all samples studied are shown in Figure 6. The zT of all samples increased with increasing temperature, as expected. The largest zT value measured was 0.60 at 1273 K for the composition with the largest effective mass, $Zn_{97}Al_2GaO_{100}$. The trends in this study are consistent with that previously reported,[23] and it results in the highest experimental zT value to-date for ZnO alloys. The previous report did not measure high temperature thermal conductivity or publish carrier concentration data to determine the amount of dopant incorporated into the lattice. Variations in the pressing conditions relative to the previous work could cause different amounts of the dopants to be incorporated, resulting in a slightly different composition with the maximum zT. Therefore, it is difficult to ascertain which nominal composition is equivalent to the one in this study. Nevertheless, the apparent anomalous result in both studies can be explained through band resonance in samples with similar amounts of dopant added to give the maximum zT. Overall, the results imply that a reduction in the lattice thermal conductivity by nanostructuring and alloying has a large effect on the thermoelectric performance. This in conjunction with resonant scattering enabled this high zT of 0.6 in the ZnO alloy.

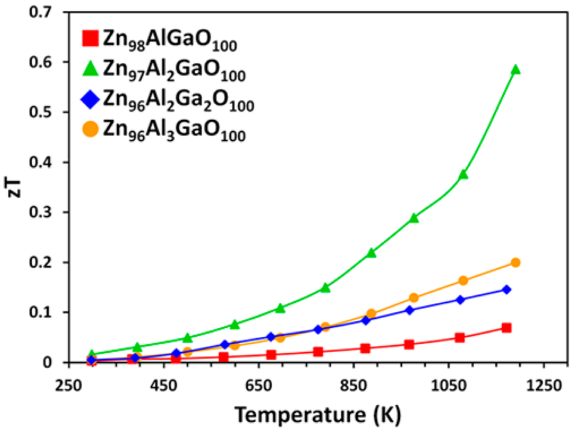

Figure 6. Plot indicating the zT variation with temperature of the dually doped ZnO samples. A peak zT of 0.6 at 1273 K was achieved at an optimally doped composition of $Zn_{97}Al_2GaO_{100}$.

■ CONCLUSIONS

Bulk assemblies of aluminum and gallium dually doped ZnO nanowires were fabricated using spark plasma sintering. These nanobulk alloys were characterized for their thermoelectric properties, and a peak zT of 0.6 was observed at a temperature of 1273 K in $Zn_{97}Al_2GaO_{100}$. This zT value is the highest experimentally reported to-date for any *n*-type oxide. The enhanced zT value of the $Zn_{97}Al_2GaO_{100}$ composition is attributed to resonant scattering coupled with the retention of nanostructuring after consolidation. Although this material still lags behind state-of-the-art thermoelectric materials in terms of thermoelectric performance, it can be synthesized into modules at a much lower cost. This makes ZnO alloys a viable cost-effective thermoelectric material option for waste-heat recovery in the terrestrial market.

MATERIALS AND METHODS

ZnO nanowires used as a raw material for this study had diameters in the 50−100 nm range, and averaged 5 μm in length. These nanowires were mass produced on a kilogram quantity scale using a microwave plasma jet reactor, a process that has been described in detail in a previous publication.[45] The fabrication of bulk pellets composed of doped ZnO nanowires involved the following steps. The as-obtained ZnO nanowires were mixed with commercially available Ga_2O_3 and Al_2O_3 nanoparticles in the required proportions in a high-energy mill (SPEX CertiPrep, 8000 M Mixer/Mill) operated at 20 Hz for 15 min.[3] The resulting powder mixtures were then transferred into a boron nitride (BN) spray-coated (obtained from ZYP coatings, Inc.) graphite die (Poco HPD-1)[46] and consolidated using spark plasma sintering (SPS). This sintering was performed at a temperature of 1200 °C and a pressure of 100 MPa for a total duration of 5 min under a vacuum of 10^{-4} Torr. A pulsed DC power supply with ON/OFF time intervals of 50 ms was employed for sintering the pellets. For consolidating and sintering the powder mixtures using SPS, the pressure and temperature were respectively ramped at 10 MPa per minute and 200 °C per minute. The same ramp rates were used while cooling the consolidated pellets. The consolidated $Zn_{1-x-y}Al_xGa_yO$ pellets were then removed from the BN coated graphite die and polished into 12 mm diameter, 1 mm thick cylindrical pellets that have flat and parallel faces. Archimedes' principle, along with coupled geometric and mass measurements, was used to measure the density of each pellet.[3] These measurements confirmed that the density of all the pellets fabricated was ≥95% of the theoretical density. To obtain reliable data, two pellets of each composition were fabricated for the measurement of their thermoelectric performance.

The characterization of the ZnO nanowires was performed using scanning electron microscopy (SEM),[47] X-ray Diffraction (XRD),[48] high-resolution transmission electron microscopy (HRTEM),[48] X-ray photoelectron spectroscopy (XPS),[47] Raman spectroscopy,[49] and photoluminescence (PL) and reported extensively in previous publications.[49] The material characterization of the highly dense pellets fabricated was also performed using XRD and HRTEM. In addition, backscattered and secondary scanning electron microscopy (SEM), and energy dispersive spectroscopy (EDS) were also employed to characterize the pellets. As-obtained pellets were directly employed for SEM, XRD, and EDS analysis of the samples. However, a destructive technique involving chipping consolidated pellets, followed by loading these chips onto TEM grids was employed for the HRTEM characterization of the pellets.[50,51]

Thermal conductivity measurements of the consolidated pellets were done in accordance with ASTM standard E1461.[52] The three parameters necessary for the determination of thermal conductivities of the pellets, density, heat capacity and thermal diffusivity, were respectively obtained using Archimedes' principle, differential scanning calorimetry (DSC) and laser flash analysis (LFA).[53] As mentioned above, the density of the pellets was determined using Archimedes' principle. LFA was performed using a Netzsch LFA 457 microflash apparatus. Both LFA and DSC were performed under dynamic vacuum conditions of 10^{-5} Torr. Thermal diffusivity and heat capacity were measured from room temperature (25 °C) to 1000 °C.[53]

The electron mobility, carrier concentration, and electrical conductivity were measured using a custom-built Hall measurement system at various temperatures ranging from room temperature to 1000 °C, and under a vacuum of 10^{-6} Torr.[54] A 1 T magnet was employed in these measurements. These measurements were performed under both positive and negative field conditions. Finally, the Seebeck coefficient was determined by measuring the voltage drop across the pellet under an applied temperature gradient.[55] These measurements were also performed at various pellet temperatures in the 25−1000 °C range, and under a 10^{-5} Torr dynamic vacuum. All of these measurements were repeated two times on each pellet, so as to ensure accuracy. From these measurements, the thermoelectric performance of the pellets as functions of their compositions and temperatures was deduced.

ASSOCIATED CONTENT

Supporting Information

Data on carrier concentration, precipitant analysis on chipped nanowire pellets and, carrier effective mass calculation based on single parabolic band model. This material is available free of charge via the Internet at http://pubs.acs.org.

AUTHOR INFORMATION

Corresponding Author

*S. Vaddiraju. Phone: 979-862-1615. Fax: 979-845-6446. E-mail: sreeram.vaddiraju@tamu.edu.

Notes

The authors declare no competing financial interest.

ACKNOWLEDGMENTS

The authors thank Dr. Jean-Pierre Fleurial and Dr. Sabah Bux of NASA JPL for providing access to the SPS and thermoelectric characterization equipment. They thank Dr. Jacek Jasinski for help with the TEM characterization of the individual nanowires and consolidated nanowire pellets. Finally, financial support from the NSF/DOE thermoelectric partnership (NSF CBET #1048702) is also gratefully acknowledged.

REFERENCES

(1) Snyder, G. J.; Toberer, E. S. Complex Thermoelectric Materials. *Nat. Mater.* **2008**, *7* (2), 105−114.

(2) Vining, C. B. An Inconvenient Truth About Thermoelectrics. *Nat. Mater.* **2009**, *8* (2), 83−85.

(3) Bux, S. K.; Yeung, M. T.; Toberer, E. S.; Snyder, G. J.; Kaner, R. B.; Fleurial, J.-P. Mechanochemical Synthesis and Thermoelectric Properties of High Quality Magnesium Silicide. *J. Mater. Chem.* **2011**, *21* (33), 12259−12266.

(4) Snyder, G. J.; Christensen, M.; Nishibori, E.; Caillat, T.; Iversen, B. B. Disordered Zinc in Zn_4Sb_3 with Phonon-Glass and Electron-Crystal Thermoelectric Properties. *Nat. Mater.* **2004**, *3* (7), 458−463.

(5) Nolas, G. S.; Morelli, D. T.; Tritt, T. M. Skutterudites: A Phonon-Glass-Electron Crystal Approach to Advanced Thermoelectric Energy Conversion Applications. *Annu. Rev. Mater. Sci.* **1999**, *29*, 89−116.

(6) Yazawa, K.; Koh, Y. R.; Shakouri, A. Optimization of Thermoelectric Topping Combined Steam Turbine Cycles for Energy Economy. *Appl. Energy* **2013**, *109* (0), 1−9.

(7) Ren, S.; Zhao, N.; Crawford, S. C.; Tambe, M.; Bulović, V.; Gradečak, S. Heterojunction Photovoltaics Using Gaas Nanowires and Conjugated Polymers. *Nano Lett.* **2010**, *11* (2), 408−413.

(8) Dresselhaus, M. S.; Lin, Y. M.; Rabin, O.; Jorio, A.; Souza Filho, A. G.; Pimenta, M. A.; Saito, R.; Samsonidze, G.; Dresselhaus, G. Nanowires and Nanotubes. *Mater. Sci. Eng., C* **2003**, *23* (1−2), 129−140.

(9) Mingo, N. Thermoelectric Figure of Merit and Maximum Power Factor in III-V Semiconductor Nanowires. *Appl. Phys. Lett.* **2004**, *84* (14), 2652−2654.

(10) Wang, W.; Jia, F. L.; Huang, Q. H.; Zhang, J. Z. A New Type of Low Power Thermoelectric Micro-Generator Fabricated by Nanowire Array Thermoelectric Material. *Microelectron. Eng.* **2005**, *77* (3−4), 223−229.

(11) Hochbaum, A. I.; Chen, R. K.; Delgado, R. D.; Liang, W. J.; Garnett, E. C.; Najarian, M.; Majumdar, A.; Yang, P. D. Enhanced Thermoelectric Performance of Rough Silicon Nanowires. *Nature* **2008**, *451* (7175), 163−U5.

(12) Boukai, A. I.; Bunimovich, Y.; Tahir-Kheli, J.; Yu, J. K.; Goddard, W. A.; Heath, J. R. Silicon Nanowires as Efficient Thermoelectric Materials. *Nature* **2008**, *451* (7175), 168−171.

(13) Rao, A. M.; Ji, X. H.; Tritt, T. M. Properties of Nanostructured One-Dimensional and Composite Thermoelectric Materials. *MRS Bull.* **2006**, *31* (3), 218−223.

(14) Taylor, S. R. Abundance of Chemical Elements in the Continental Crust - A New Table. *Geochim. Cosmochim. Acta* **1964**, *28* (8), 1273−1285.

(15) Fergus, J. W. Oxide Materials for High Temperature Thermoelectric Energy Conversion. *J. Eur. Ceram. Soc.* **2012**, *32* (3), 525−540.

(16) Van Nong, N.; Pryds, N.; Linderoth, S.; Ohtaki, M. Enhancement of the Thermoelectric Performance of P-Type Layered Oxide $Ca_3Co_4O_{9+\Delta}$ through Heavy Doping and Metallic Nanoinclusions. *Adv. Mater.* **2011**, *23* (21), 2484−2490.

(17) Ito, M.; Furumoto, D. Microstructure and Thermoelectric Properties of $Na_xCo_2O_4$/Ag Composite Synthesized by the Polymerized Complex Method. *J. Alloys Compd.* **2008**, *450* (1−2), 517−520.

(18) Kikuchi, A.; Okinaka, N.; Akiyama, T. A Large Thermoelectric Figure of Merit of La-Doped $SrTiO_3$ Prepared by Combustion Synthesis with Post-Spark Plasma Sintering. *Scr. Mater.* **2010**, *63* (4), 407−410.

(19) Cai, K. F.; Muller, E.; Drasar, C.; Mrotzek, A. Preparation and Thermoelectric Properties of Al-Doped ZnO Ceramics. *Mater. Sci. Eng., B* **2003**, *104* (1−2), 45−48.

(20) Tsubota, T.; Ohtaki, M.; Eguchi, K.; Arai, H. Thermoelectric Properties of Al-Doped Zno as a Promising Oxide Material for High-Temperature Thermoelectric Conversion. *J. Mater. Chem.* **1997**, *7* (1), 85−90.

(21) Katsuyama, S.; Takagi, Y.; Ito, M.; Majima, K.; Nagai, H.; Sakai, H.; Yoshimura, K.; Kosuge, K. Thermoelectric Properties of (Zn1-yMgy)(1-x)AlxO Ceramics Prepared by the Polymerized Complex Method. *J. Appl. Phys.* **2002**, *92* (3), 1391−1398.

(22) Yamaguchi, H.; Chonan, Y.; Oda, M.; Komiyama, T.; Aoyama, T.; Sugiyama, S. Thermoelectric Properties of Zno Ceramics Co-Doped with Al and Transition Metals. *J. Electron. Mater.* **2011**, *40* (5), 723−727.

(23) Ohtaki, M.; Araki, K.; Yamamoto, K. High Thermoelectric Performance of Dually Doped ZnO Ceramics. *J. Electron. Mater.* **2009**, *38* (7), 1234−1238.

(24) Yoon, M. H.; Lee, S. H.; Park, H. L.; Kim, H. K.; Jang, M. S. Solid Solubility Limits of Ga and Al in ZnO. *J. Mater. Sci. Lett.* **2002**, *21* (21), 1703−1704.

(25) Palmer, G. B.; Poeppelmeier, K. R. Phase Relations, Transparency and Conductivity in Ga_2O_3-SnO_2-ZnO. *Solid State Sci.* **2002**, *4* (3), 317−322.

(26) Colinas, J. M. F.; Areán, C. O. Kinetics of Solid-State Spinel Formation: Effect of Cation Coordination Preference. *J. Solid State Chem.* **1994**, *109* (1), 43−46.

(27) Munir, Z.; Anselmi-Tamburini, U.; Ohyanagi, M. The Effect of Electric Field and Pressure on the Synthesis and Consolidation of Materials: A Review of the Spark Plasma Sintering Method. *J. Mater. Sci.* **2006**, *41* (3), 763−777.

(28) Cao, G.; Wang, Y. *Nanostructures and Nanomaterials: Synthesis, Properties, and Applications*, 2nd ed.; World Scientific: Singapore, 2011.

(29) Noh, J.-Y.; Kim, H.; Kim, Y.-S.; Park, C. H. Electron Doping Limit in Al-Doped Zno by Donor-Acceptor Interactions. *J. Appl. Phys.* **2013**, *113* (15), 153703−153705.

(30) Hansson, R.; Hayes, P.; Jak, E. Experimental Study of Phase Equilibria in the Al-Fe-Zn-O System in Air. *Metall. Mater. Trans. B* **2004**, *35* (4), 633−642.

(31) Hu, J.; Gordon, R. G. Textured Aluminum-Doped Zinc Oxide Thin Films from Atmospheric Pressure Chemical-Vapor Deposition. *J. Appl. Phys.* **1992**, *71* (2), 880−890.

(32) Hu, J.; Gordon, R. G. Atmospheric Pressure Chemical Vapor Deposition of Gallium Doped Zinc Oxide Thin Films from Diethyl Zinc, Water, and Triethyl Gallium. *J. Appl. Phys.* **1992**, *72* (11), 5381−5392.

(33) Jaworski, C. M.; Kulbachinskii, V.; Heremans, J. P. Resonant Level Formed by Tin in Bi_{2}Te_{3} and the Enhancement of Room-Temperature Thermoelectric Power. *Phys. Rev. B* **2009**, *80* (23), 233201.

(34) Heremans, J. P.; Jovovic, V.; Toberer, E. S.; Saramat, A.; Kurosaki, K.; Charoenphakdee, A.; Yamanaka, S.; Snyder, G. J. Enhancement of Thermoelectric Efficiency in Pbte by Distortion of the Electronic Density of States. *Science* **2008**, *321* (5888), 554−557.

(35) Heremans, J. P.; Wiendlocha, B.; Chamoire, A. M. Resonant Levels in Bulk Thermoelectric Semiconductors. *Energy Environ. Sci.* **2012**, *5* (2), 5510−5530.

(36) Anderson, J.; Chris, G. V. d. W. Fundamentals of Zinc Oxide as a Semiconductor. *Rep. Prog. Phys.* **2009**, *72* (12), 126501.

(37) Imai, Y.; Watanabe, A. Comparison of Electronic Structures of Doped Zno by Various Impurity Elements Calculated by a First-Principle Pseudopotential Method. *J. Mater. Sci.: Mater. Electron.* **2004**, *15* (11), 743−749.

(38) Imai, Y.; Watanabe, A.; Shimono, I. Comparison of Electronic Structures of Doped Zns and ZnO Calculated by a First-Principle Pseudopotential Method. *J. Mater. Sci.: Mater. Electron.* **2003**, *14* (3), 149−156.

(39) Tsidil'kovskiĭ, I. M. Zero-Gap Semiconductors with Magnetic Impurities Forming Resonance Donor States. *Soviet Phys.−Uspekhi* **1992**, *35* (2), 85.

(40) Andrew, F. M.; Snyder, G. J. Introduction to Modeling Thermoelectric Transport at High Temperatures. In *Materials, Preparation, and Characterization in Thermoelectrics*; Rowe, D. M., Ed.; CRC Press: Boca Raton, FL, 2012; pp 1−18.

(41) Sze, S. M.; Ng, K. K. *Physics of Semiconductor Devices*, 3 ed.; John Wiley & Sons: New York, 2007.

(42) Fistul', V. I. *Heavily Doped Semiconductors*; Plenum Press: New York, 1969.

(43) Baer, W. S. Faraday Rotation in Zno: Determination of the Electron Effective Mass. *Phys. Rev.* **1967**, *154* (3), 785−789.

(44) Alvarez-Quintana, J.; Martinez, E.; Perez-Tijerina, E.; Perez-Garcia, S. A.; Rodriguez-Viejo, J. Temperature Dependent Thermal Conductivity of Polycrystalline ZnO Films. *J. Appl. Phys.* **2010**, *107* (6), 063713−4.

(45) Kumar, V.; Kim, J. H.; Pendyala, C.; Chernomordik, B.; Sunkara, M. K. Gas-Phase, Bulk Production of Metal Oxide Nanowires and Nanoparticles Using a Microwave Plasma Jet Reactor. *J. Phys. Chem. C* **2008**, *112* (46), 17750−17754.

(46) Bux, S. K.; Zevalkink, A.; Janka, O.; Uhl, D.; Kauzlarich, S.; Snyder, J. G.; Fleurial, J.-P. Glass-Like Lattice Thermal Conductivity and High Thermoelectric Efficiency in Yb_9Mn_(4.2)Sb_9. *J. Mater. Chem. A* **2014**, *2* (1), 215−220.

(47) Hassan, H. H.; Amin, M. A.; Gubbala, S.; Sunkara, M. K. Participation of the Dissolved O_2 in the Passive Layer Formation on Zn Surface in Neutral Media. *Electrochim. Acta* **2007**, *52* (24), 6929−6937.

(48) Petzold, F. G.; Jasinski, J.; Clark, E. L.; Kim, J. H.; Absher, J.; Toufar, H.; Sunkara, M. K. Nickel Supported on Zinc Oxide Nanowires as Advanced Hydrodesulfurization Catalysts. *Catal. Today* **2012**, *198* (1), 219−227.

(49) Chakrapani, V.; Pendyala, C.; Kash, K.; Anderson, A. B.; Sunkara, M. K.; Angus, J. C. Electrochemical Pinning of the Fermi Level: Mediation of Photoluminescence from Gallium Nitride and Zinc Oxide. *J. Am. Chem. Soc.* **2008**, *130* (39), 12944−12952.

(50) Brockway, L.; Vasiraju, V.; Vaddiraju, S. Compositional Disorder and Its Effect on the Thermoelectric Performance of Zn_3P_2 Nanowire−Copper Nanoparticle Composites. *Nanotechnology* **2014**, *25* (12), 125402.

(51) Brockway, L.; Vasiraju, V.; Asayesh-Ardakani, H.; Shahbazian-Yassar, R.; Vaddiraju, S. Thermoelectric Properties of Large-Scale Zn_3P_2 Nanowire Assemblies. *Nanotechnology* **2014**, *25* (14), 145401.

(52) ASTM. Standard Test Method for Thermal Diffusivity by the Flash Method. *ASTM Standard E1461*; ASTM: West Conshohocken, PA, 2001; pp 458−469.

(53) Yi, T.; Zhang, G.; Tsujii, N.; Fleurial, J.-P.; Zevalkink, A.; Snyder, G. J.; Grønbech-Jensen, N.; Kauzlarich, S. M. Phase Characterization, Thermal Stability, High-Temperature Transport Properties, and Electronic Structure of Rare-Earth Zintl Phosphides $Eu_3M_2P_4$ (M = Ga, in). *Inorg. Chem.* **2013**, *52* (7), 3787−3794.

(54) Borup, K. A.; Toberer, E. S.; Zoltan, L. D.; Nakatsukasa, G.; Errico, M.; Fleurial, J.-P.; Iversen, B. B.; Snyder, G. J. Measurement of the Electrical Resistivity and Hall Coefficient at High Temperatures. *Rev. Sci. Instrum.* **2012**, *83*, (12). DOI: 10.1063/1.4770124.

(55) Wood, C.; Zoltan, D.; Stapfer, G. Measurement of Seebeck Coefficient Using a Light Pulse. *Rev. Sci. Instrum.* **1985**, *56* (5), 719–722.